

# Study of the Effect of Process Parameters and Heat Treatment on the Formation and Evolution of Directed Energy Deposition of IN718-CuCrZr Interface

Hamidreza Javidrad and Bahattin Koc\*

Joining dissimilar materials as coatings or multimaterial compounds remains challenging due to mismatches in atomic orientation, microstructure, and thermal properties. The laser powder directed energy deposition (LP-DED) process is an additive manufacturing (AM) technique capable of producing bimetallic or functionally graded materials for coatings or heavy-duty applications. However, understanding interface characteristics in response to process parameters and heat treatment is critical for evaluating structural integrity. This study investigates the Inconel 718/CuCrZr interface and examines the effects of process parameters and heat treatment on microstructural evolution. The optimized bimetallic sample is free of cracks and excessive porosity, indicating a successful deposition. The results show that Inconel 718 acts as a thermal barrier during CuCrZr deposition due to its low thermal conductivity, significantly influencing grain structure and hardness. To achieve a homogeneous interface, four heat treatment strategies are used, and their effects on microstructure and hardness are analyzed. These strategies induce major changes in joint properties, demonstrating that an appropriate heat treatment improves hardness, interface characteristics, and microstructural uniformity. The findings confirm that achieving the desired interface properties for coatings or multimaterial production is possible through optimized process parameters and heat treatment.

methods. AM processes are based on layer-by-layer production of a complex geometry directly from a CAD model; thus, near-net shape products can be produced through this technology.<sup>[1]</sup> AM of metals has already been recognized as a reliable method for producing high-value and heavy-duty mechanical components such as combustion chambers, conformal cooling channels, and turbine blades.<sup>[2]</sup> Each metal AM technique presents unique characteristics that can significantly boost production by minimizing tooling, post-processing, and eliminating material waste.<sup>[3]</sup> Among the metal AM processes, laser powder directed energy deposition (LP-DED) has a unique position due to its higher build rate, high degree of freedom, less sensibility to the powder feedstock, and built-in capability of producing multimaterial components. The LP-DED uses a nozzle to deliver powder flow to the build plate, where a laser beam deposits the powder on the surface. Due to the use of a powder flow as the delivery system, it is feasible to combine different types of powders with exact ratios to obtain specific properties at desired locations. This unique capability combined with an unconstrained deposition strategy can be used in various industries to optimize two or more contradicting properties and boost performance and efficiency at the same time.<sup>[4]</sup> Thus, the location-dependent material composition aids in better performance and lower price, especially for high-temperature applications.

## 1. Introduction


Additive manufacturing (AM) is an emerging technology that provides several advantages over conventional manufacturing

Manufacturing of multimaterial components brings higher efficiency and performance by carefully designing the material composition at each specific location.<sup>[5]</sup> However, due to the dissimilarity of alloys in coefficient of thermal expansion (CTE) and crystal structure, specific considerations should be taken to successfully join two or more alloys together.<sup>[6]</sup> This issue requires close control of processing parameters, the composition of alloys at every location, and the knowledge of phase formation based on the composition and temperature. However, the lack of knowledge about the effect of process parameters and heat treatment on the formation and evolution of the interface is the main obstacle in the production of reliable multimaterial components.

Granting a perfect bonding between two materials has been an issue since industry associates started to weld two dissimilar materials to each other.<sup>[7]</sup> Several challenges including process control, material compatibility, complex thermodynamics within

H. Javidrad, B. Koc  
Faculty of Engineering and Natural Sciences  
Sabanci University  
34956 Istanbul, Turkey  
E-mail: bahattinkoc@sabanciuniv.edu

H. Javidrad, B. Koc  
Integrated Manufacturing Technologies Research and Application Center  
Sabanci University  
34956 Istanbul, Turkey

 The ORCID identification number(s) for the author(s) of this article can be found under <https://doi.org/10.1002/adem.202500773>.

© 2025 The Author(s). Advanced Engineering Materials published by Wiley-VCH GmbH. This is an open access article under the terms of the Creative Commons Attribution License, which permits use, distribution and reproduction in any medium, provided the original work is properly cited.

DOI: 10.1002/adem.202500773

the interface, intermetallic formation, and cracking need to be tackled in order to achieve a successful production. Since a wide range of alloys are now available and compositionally tailored to be used as powder feedstock for the LP-DED process, many researchers have tried different combinations of these alloys to understand the phenomena behind a successful joining.<sup>[8]</sup> Cu-based alloys gained significance due to their superior thermal conductivity and oxidation resistivity,<sup>[9,10]</sup> especially in heat exchangers and cooling channels; however, their low mechanical properties intensify the desire to reinforce it with high-strength alloys, especially Inconel series, to obtain a component that can withstand very high temperatures, as well as dissipate heat faster.<sup>[11,12]</sup> To highlight the positive impact of copper on the performance of heavy-duty components, Oniuke et al.<sup>[13]</sup> achieved  $\approx 250\%$  and  $\approx 300\%$  increase in thermal diffusivity and thermal conductivity, respectively, by producing 50–50 gradient GRCop-84/Inconel 718 in comparison to pure Inconel 718. Note that the printability of Cu-based alloys has other issues including high reflectivity and low absorptivity, which require close control of process parameters.<sup>[14]</sup>

Inconel 718 (IN718) is a nickel-based solid-solution alloy with a wide range of applications in high-temperature environments. The strengthening phase in IN718 is  $\gamma' + \gamma''$  mainly consisting of  $\text{Ni}_3(\text{Nb}, \text{Ti}, \text{Al})$ , along with Laves,  $\delta$ , and MC carbides.<sup>[15]</sup> This alloy is known for its excellent high-temperature performance in terms of strength, oxidation, corrosion, and creep resistance.<sup>[16]</sup> On the other hand, CuCrZr is a precipitation-hardened copper-based alloy with improved strength and high thermal conductivity, which has gained many applications in the production of heat exchangers, combustion chamber parts, and cooling channels.<sup>[17]</sup> The role of Cr in this alloy is to add heat absorptivity and mechanical strength to copper, while the Zr element is to enhance powder flowability and strength.<sup>[18,19]</sup> The combination of these two alloys can significantly increase the mechanical and thermal performance of heavy-duty components in critical applications. Therefore, it is highly desirable to investigate the mechanics of fusion between these alloys in order to tailor the microstructural, mechanical, and thermal properties of such multimaterial components.

Characterization of the Inconel-copper interface has a considerable history; however, the effect of processing and post-processing parameters on the formation of the interface is still under investigation. Anderson et al.<sup>[20]</sup> deposited Inconel 625 on C18150 via the LP-DED process and observed a large interfacial region resulting from the high diffusion rate during this process. Zhang et al.<sup>[21]</sup> studied the feasibility of the utilization of CuCr alloy as substrate in LP-DED of 07Cr15Ni5 steel. It was revealed that the required energy for a successful deposition is excessively high for this particular case. The reason was reported to be the high thermal conductivity of copper alloy, which causes rapid cooling and insufficient melt pool. Further, Liu et al.<sup>[22]</sup> and Mao et al.<sup>[23]</sup> also observed vertical cracks within the interface of deposited C18400 and CuCrZr alloys on 316L stainless steel due to the excessive applied energy and crystallographic incompatibility, which led to micro residual stress and separation. Chen et al.<sup>[24–26]</sup> reported cracks within the interface of CuSn10 (bronze) and 316L stainless steel bimetallic samples produced using the laser powder bed fusion (L-PBF) process. A diffusion layer is a common observation in the Cu–Fe interface.<sup>[25]</sup>

It was also shown that insufficient energy caused cracking and delamination in the horizontal direction, while excessive energy generated vertical cracks, which may result from the difference in thermal expansion of the two materials.<sup>[25]</sup> Recently, Yang et al.<sup>[27]</sup> achieved a crack-free interface while depositing CuCrZr on AlSi7Mg through the use of a coaxial infrared-blue hybrid laser with a low-power infrared laser. However, this type of system is expensive and not widely available. Mishra et al.<sup>[28]</sup> investigated the interface characteristics of wire and arc additively manufactured (WAAM) Inconel 718 and Ti-6Al-4V with CuSi as the interfacial bonding alloy.  $\text{Cu}_4\text{Ti}_3$ ,  $\text{Cu}_3\text{Ti}_2$ ,  $\text{Cu}_4\text{Ti}$ ,  $\text{CuTi}_2$ , and  $\text{Ti}_5\text{Si}_3$  were phases that formed within the Cu–Ti interface, whereas CuNi and  $\text{NiCr}_2$  phases at the Ni–Cu interface. Zhang et al.<sup>[6]</sup> used Inconel 718 as the bonding alloy between 316L stainless steel and pure copper. The results showed a better defect-free bonding can be achieved through the use of IN718 as the interlayer alloy. Pan et al.<sup>[29]</sup> produced a defect-free bimetallic part composed of Inconel 625 and pure copper and studied the interface properties. Cabibbo et al.<sup>[30]</sup> investigated the feasibility of producing CuCrZr-Tungsten FGM for intense working environments. Even though the effort turned out to be successful, the induced residual stress within the interface was not negligible. Thus, apart from the defect-free bonding, it is important to evaluate the state of residual stress to avoid unpredictable failure.

Heat treatment is a common solution to fix the microstructural and mechanical heterogeneity of metal AM products, as well as to relieve excessive residual stress.<sup>[31]</sup> In the case of pure materials, standard heat treatment strategies are available according to the required properties for each application. This also gains significance due to the wide variation in the characteristics of additively joined materials. The growing desire for the utilization of multimaterial components requires an understanding of the effect of heat treatment on the interfacial region of the two materials. However, there are only a few examples in the literature dealing with the effect of heat treatment on the microstructural and mechanical evolution of bimetallic components, especially in the vicinity of the interface. Liu et al.<sup>[32]</sup> demonstrated the effect of heat treatment on the microstructure and properties of bronze-steel bimetallic structures. It was found that the used heat treatment led to grain reorientation and microstructure homogenization. On the other hand, heat treatment resulted in lower residual stress and dislocation density leading to a lower mechanical strength. Li et al.<sup>[33]</sup> studied the effect of heat treatment on the microstructure and fracture behavior of LP-DED SS316L/IN718 bimetallic samples. It was shown that the length of the diffusion zone increased after the heat treatment and revealed a gradual elemental change in the deposition direction. Severe recrystallization occurred on the SS316L side of the interface while the microstructure of the IN718 side remained unchanged. Further, the mechanical properties of the bimetallic samples enhanced upon applying heat treatment.

In this article, the effect of process parameters and heat treatment on the LP-DED bimetallic IN718-CuCrZr interface formation and evolution were investigated for the first time. To this goal, process parameter optimization was carried out specifically for the mentioned structure to obtain a flawless and strong interface. The common heat treatment strategies for IN718 and CuCrZr were used to design a unique heat treatment for the

bimetallic structure. Detailed investigation including microstructural and mechanical analyses were carried out to identify the effect of each heat treatment on the interface, as well as the individual IN718 and CuCrZr. Suitability of the optimum heat treatment strategy was evaluated based on the microstructural homogeneity, phase analysis, and hardness improvement for both involved materials.

## 2. Experimental Section

### 2.1. Powder Feedstocks

For the present study, gas atomized CuCrZr powder with a particle size of 45–106  $\mu\text{m}$  and Inconel 718 (IN718) with a particle diameter of 70–120  $\mu\text{m}$  was supplied from SENTES BIR (Turkey) and Oerlikon (USA), respectively. **Figure 1a,b** show the SEM images of the raw powders. Powder size distribution was calculated from low-magnification SEM images and represented in **Figure 1c,d**. Three frames from each material were analyzed to ensure over 100 particle measurements. **Table 1** reflects the composition of the two raw materials adapted from the data sheets.

### 2.2. LP-DED Machine

A DMG Mori LASERTEC 65 hybrid machine was used for the production of the bimetallic samples. The available machine was equipped with a 2.5 kW continuous fiber laser with a

**Table 1.** The powder composition of two materials (wt%).

Material	Ni	Fe	Cr	Zr	Ti	Al	Nb	Mo	Cu
Inconel 718	Bal.	18	19	–	1	0.5	5	6	–
CuCrZr	–	–	0.87	0.06	–	–	–	–	Bal.

wavelength of 1064 nm and a spot diameter of 1.6 mm. Two hoppers were integrated into the machine to deliver powders to the base material through a coaxial nozzle known as the COAX14 manufactured by Fraunhofer, Germany. Argon was used as the shielding and carrier gas in order to protect the melt pool from oxidation. The substrate for this study was made from C45 steel with a thickness of 10 mm. No substrate pre-heating was applied prior to the deposition.

### 2.3. Sample Preparation

The design of samples and process planning was carried out in the Rhino 3D software with a developed process planning algorithm in Grasshopper to be able to modify process parameters where necessary. The overall dimension of samples was  $15 \times 15 \times 20 \text{ mm}^3$ , which were divided into two sections, as shown in **Figure 2a**. A  $3 \times 3$  full factorial design of experiment was used to study the effect of laser power and scan speed on the mechanics of the interface by producing nine samples from the

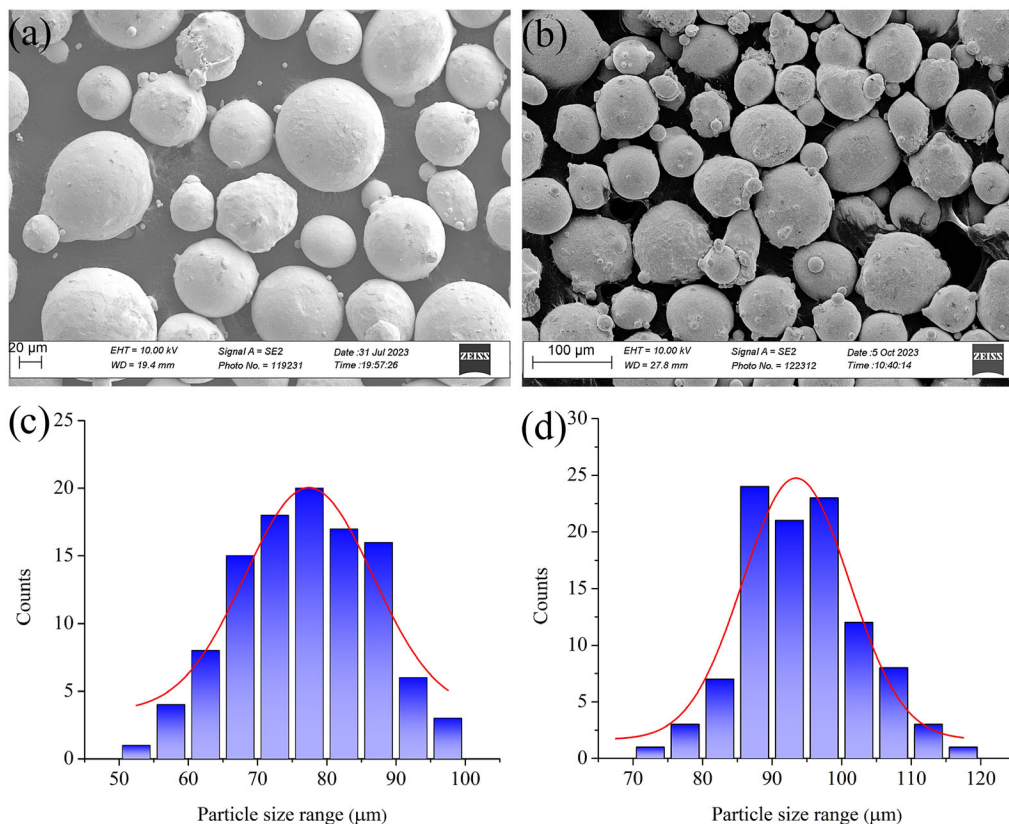


**Figure 1.** SEM images of the supplied powders and the respective particle size distribution analysis: a,c) CuCrZr and b,d) IN718.

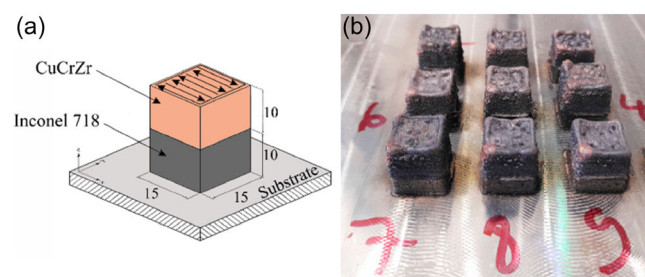


**Figure 2.** a) Schematic of the bimetallic sample and b) the produced samples.

mentioned process parameters listed in **Table 2**. The laser power should be modified layer by layer in order to avoid overheat although it can be kept constant after the 8th layer for IN718 and 10th layer for CuCrZr since the overall thermal condition of the part reaches a steady state. The scan pattern for both materials was zigzag with 0° and 90° rotation followed by a contour scan. Prior to the deposition of the second material, the as-built surface of IN718 was machined to specifically investigate the effect of process parameter selection on the waviness of the interface after the deposition of the second material. Figure 2b shows the produced samples for the interface optimization. In the subsequent step, four samples were produced using the optimum process parameters for further experiments and investigations.

In order to investigate the effect of heat treatment on the interface evolution, microstructural, and mechanical properties, four heat treatment strategies were used as demonstrated in **Table 3**,

and the results were compared to the as-built condition. The heat treatment strategies were selected according to the recommended procedures for each material.<sup>[34,35]</sup>

Heat treatments were conducted in a vacuum furnace in order to avoid oxidation, especially for CuCrZr alloy. Since two materials are involved in this study, it is impossible to perform the standard heat treatment strategy for both of them, simultaneously. Therefore, four combinations of the standard heat treatments for each material were selected to study the microstructural and mechanical evolution of the bimetallic samples. At first, a typical strategy for IN718 was used, which requires higher temperatures. Then, a low-temperature heat treatment was applied to satisfy the CuCrZr requirements. Air cooling (AC) and furnace cooling (FC) were used at 250 and 50 °C h<sup>-1</sup>, respectively. FC was applied in most of the cases in order to ensure effective precipitation of Cr within the copper alloy.<sup>[36]</sup> Table 3 shows the heat treatment strategies used in this study.

After the production, the samples were prepared for microstructural analyses. Due to the large difference between the hardness of the two materials, grinding and polishing of the interfacial area were carefully carried out in multiple steps. Electrochemical etching was used for IN718 in order to reveal the microstructure using a solution (i.e., Kalling's No. 2) composed of 100 mL HCl, 100 mL ethanol, and 5 g CuCl<sub>2</sub> with a voltage of 5 V for 5 s. For the CuCrZr section, regular chemical etching with a solvent consisting of 100 mL ethanol, 25 mL HCl, and 5 gr ferric II chloride was used. Nevertheless, it is not possible to properly etch the inter-fusion zone due to the low corrosion resistivity of the copper alloy to the high-concentration acid used for the IN718.

**Table 2.** Process parameters for material deposition.

Material	Inconel 718	CuCrZr
Laser power [W]	Start from 1067 and decreased 50 W per layer until 8th layer	600/700/800 for three layers, then increase 100 W per layer until 10th layer
Scan speed [mm min <sup>-1</sup> ]	1000	500/750/900
Powder feed rate [g min <sup>-1</sup> ]	9	4.5
Carrier gas flow [L min <sup>-1</sup> ]	3.1	2
Shield gas [L min <sup>-1</sup> ]	5	10
Layer thickness [mm]	1.12	0.85
Overlap ratio [%]	50	60
Dwell time [s]	9	9

## 2.4. Characterization

An ordinary optical microscope (OM) was used for general inspection of the polished surfaces of the samples. A Zeiss Gemini field emission scanning electron microscope (FESEM) equipped with an EDAX X-ray electron-dispersive spectroscopy (EDS) detector and an electron backscatter diffraction (EBSD) camera were used for an in-detail study of the interface. Prior to the EBSD analysis, the samples were polished using a DLyte ion polishing machine in order to remove the surface stress caused by the mechanical polishing.

Vickers microhardness (HV1) test was carried out along the build direction on ±6 mm in the vicinity of the interface with 0.5 mm intervals. Prior to the test, the subjective surface was carefully polished and cleaned. The used machine was a multipurpose hardness tester with automated testing and measurement

**Table 3.** Heat treatment strategies and their applications.

Title	Description	Purpose
Direct aging (HT1)	480 °C × 2 h/FC	Solid-solution precipitation of CuCrZr
Solution annealing + aging (HT2)	980 °C × 2 h/FC + 480 °C × 2 h/FC	Recrystallization and homogenization for IN718 and CuCrZr
Solution annealing (HT3)	1080 °C × 1 h/FC	Solution annealing and recrystallization for IN718
Solution annealing + triple aging (HT4)	1080 °C × 1 h/AC + 760 °C × 10 h/FC + 650 °C × 8 h/FC + 480 °C × 2 h/AC	Standard heat treatment for IN718 to increase strength and direct aging for CuCrZr



capability; however, manual evaluation of the measurements was also carried out for the validation of the results.

### 3. Results and Discussions

#### 3.1. OM Analysis

**Figure 3** shows the schematic of the formation mechanism of the interface along with the actual interface between the IN718 and CuCrZr. The overall analysis revealed that only a few defects existed in the vicinity of the interface, especially within the IN718 section. No sign of cracking was observed within the interface, which is a promising indication of a successful bonding. Since a high input energy was used to overcome the low laser absorptivity of CuCrZr alloy, it caused the IN718 to be extensively remelted during the deposition of the initial CuCrZr layers. Due to the lower mass density of IN718 and the Marangoni convection effect, the molten material migrated to the upper level and solidified within the CuCrZr matrix. Since the solidification point of IN718 is higher, there is not enough time for the spherical morphologies to coalesce and form larger clusters. Also note that decreasing the input heat leads to fewer disruptions and smaller islands. The same phenomenon was previously observed when depositing CuCrZr on stainless steel 316L or IN718 via the L-PBF process.<sup>[5,23,37]</sup> Furthermore, Dang et al.<sup>[38]</sup> elaborated that this phenomenon can be engineered to improve the bonding within the interface for dissimilar materials through formation of fish scale morphologies.

#### 3.2. Effect of Laser Power and Scan Speed

The formation of an effective fusion interface is directly affected by the selection of process parameters. Since the laser power and scan speed have significant impacts on the input heat, these parameters are the key factors that play a major role in the formation of the interface. Zhang et al.<sup>[39]</sup> reported that an increase in laser power leads to an increase in the depth of the Marangoni flow, which causes more transportation of molten material from the base material to the upper levels. Mao et al.<sup>[23]</sup> also confirmed this statement for the L-PBF of 316L/CuCrZr interface.

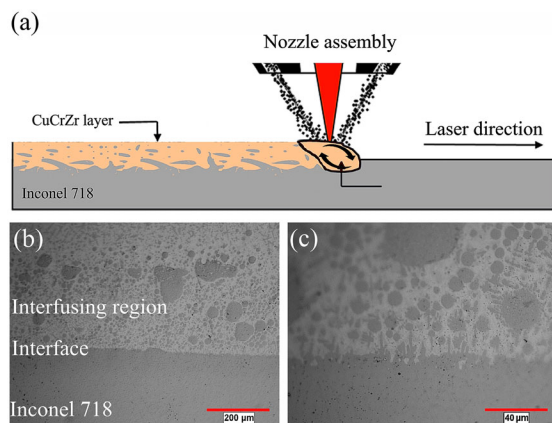


**Figure 3.** Formation of IN718/CuCrZr interface: a) schematic and b,c) optical micrographs.

Furthermore, it was found that increasing the scan speed tends to yield less disruption until a specific point above which the interface starts to get wavy again due to the lack of proper adhesion. Note that the optimum stepover should also be selected in order to avoid excessive input heat. Chen et al.<sup>[25]</sup> observed that the width of the interfacial region is significantly affected by the scan speed rather than laser power. Koukolíková et al.<sup>[40]</sup> showed that higher laser power increases the interface width by providing higher input heat for mass transport. However, the interface waviness decreased by increasing the laser power.

**Figure 4** shows the SEM images from the interface of the produced samples using different combinations of laser power and scan speed. As shown, all the samples revealed a crack-free interface, while the porosity content varied according to the process parameter variations. Changing the laser power and scan speed led to two distinct effects on the formation of the interface. The first effect is the interface disturbance or waviness and the second effect is the mass transport due to the difference in the mass density of the materials. Increasing the laser power with constant scan speed causes an increase in the depth of the Marangoni flow and higher interface disruption. The only solution for this is to increase the scan speed to compensate for the effect of high energy density, as depicted in case #6. From the scan speed perspective, higher scan speed tends to generate a shallow melt pool and less heat penetration; therefore, the obtained interface was smoother; unless the laser power was high enough to cause disruption on a larger scale, as seen in case #9. Increasing scan speed with the same level of laser power leads to less fish scale effect and more spherical mass transport due to the formation of a shallow melt pool. Interface waviness resulting from the intense heat penetration can cause gas entrapment and porosity formation, as occurred in some cases (i.e., #3, 5, and 9). The fish scale effect is challenging to control and causes inconsistent properties along the interface; however, it provides better bonding between the two materials. Therefore, a tradeoff between the spherical and fish scale fusion zones with the least interface waviness is preferred. According to the obtained results, specimen #6 showed a controlled formation of fish scales and spherical particles, along with low waviness, which is considered as the optimum case. Note that the obtained process parameters are only valid for the production of the interface and the laser power should be increased for CuCrZr after the deposition of a few layers to overcome the low wettability and high reflectivity of copper. In the produced samples, the laser power increased with a 100 W increment after the third layer; therefore, the samples can be produced without affecting the interface condition.

#### 3.3. SEM Analysis

Detailed SEM analysis was carried out for the optimum sample (i.e., Sample #6) in the as-built and heat-treated conditions. **Figure 5** shows the microstructure of the optimum as-built sample at different locations. In the CuCrZr side (shown in Figure 5a–c), solid-solution Cr elements with a diameter ranging from 0.4 to 1 μm were precipitated due to the low cooling rate during the deposition. This microstructure is specific to the LP-DED process while no or slight Cr precipitation was observed during the L-PBF of this alloy.<sup>[41]</sup>

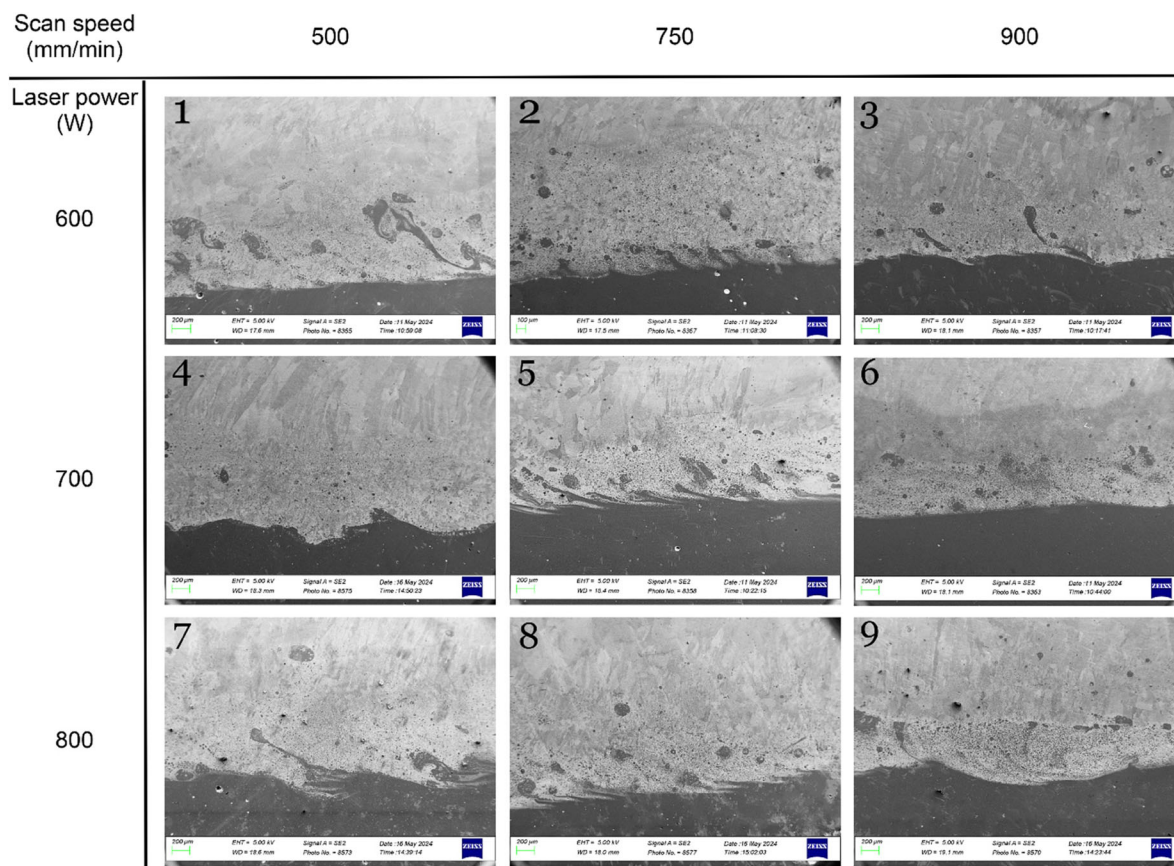


**Figure 4.** The SEM micrographs from the interface of IN718 and CuCrZr produced using different process parameters.

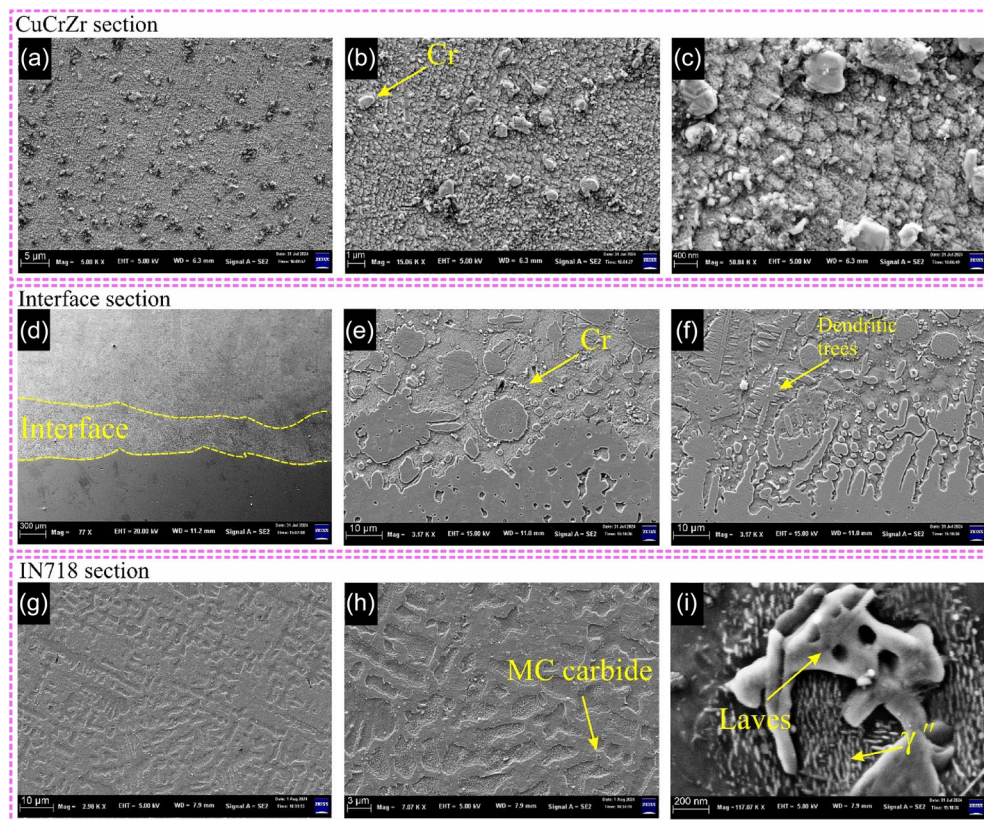
Figure 5d–f show the interface between CuCrZr and IN718. As observed in the previous section, the interface revealed an uneven fusion line caused by the Marangoni convection of IN718 to the CuCrZr side. Figure 5e shows the Cr element was precipitated within the grain boundaries of CuCrZr, which resulted from prolonged heating of this region. The morphology of IN718 within the fusion zone consists of dendritic trees and spherical regions at a wide range of dimensions shown in Figure 5f. The dendritic trees were usually connected to the base IN718 material and elongated throughout the heat dissipation direction. Nevertheless, excessive thermal stress can cause free dendrite formation, as shown in Figure 5f. The origin of these structures is mainly the difference between the cooling rates and the solidification temperature of the two materials.<sup>[42]</sup> This usually happens when the cooling rate is higher than  $10^4 \text{ K s}^{-1}$  causing undercooling of the melted material before nucleation.<sup>[43]</sup> Lower solidification temperature for CuCrZr (i.e., 1065–1080 °C) allowed IN718 to grow within the liquid copper matrix and form the dendritic trees.

Figure 5g–i show the SEM micrographs from the IN718 region of the bimetallic sample. The microstructure of IN718 revealed the formation of a dense interdendritic region, with the existence of solid-solution MC carbides and the Laves phase. A low cooling rate during the deposition of CuCrZr provided more time for the primary dendritic arms to extend almost triple the size (i.e., 3  $\mu\text{m}$ ) compared to the single material deposition.<sup>[44]</sup> The MC carbides

can be found all over the surface and their composition is mainly Ti, Ta, and Nb.<sup>[44]</sup> The Laves phase was formed within the interdendritic region and mainly contained Nb, Cr, and Mo elements. The width of the Laves precipitates was 1  $\mu\text{m}$  on average. This phase is generally formed due to the high content of Nb segregated during the solidification phase of the LP-DED process.<sup>[45]</sup> Comparing to the pure IN718 specimen produced using the same processing condition,<sup>[44]</sup> the Laves phase showed a reduction in aspect ratio; therefore, the prolonged deposition of CuCrZr provided a favorable condition for the evolution of this phase from elongated into blocky Laves. The same effect was observed by Sreekanth et al.<sup>[46]</sup> after solution treatment of LP-DED IN718 at 954 °C for 1 h followed by air-cooling process. Note that there was no sign of the gamma prime ( $\gamma'$ ) phase because of the low content of Al and Ti, while the gamma double prime ( $\gamma''$ ) phase was detected at a submicron level in Figure 5i. Since the formation of the  $\gamma''$  phase depends on the time and temperature,<sup>[47]</sup> it was also expected to find signs of this phase after the deposition of CuCrZr on the IN718 sample.

Figure 6a–c show the microstructural evolution of the bimetallic sample after the HT1 heat treatment. It can be seen in Figure 6a that the direct aging caused precipitate coarsening for CuCrZr alloy. The direct aging in HT1 increased the population and size of the precipitation hardening phase up to 2  $\mu\text{m}$ , which contains a large amount of Cr. Wang et al.<sup>[48]</sup> found that solution annealing causes recrystallization and a decrease in the





**Figure 5.** SEM images of the side surface of the bimetallic sample: a–c) CuCrZr region, d–f) interface region, and g–i) IN718 region.

mechanical properties of CuCrZr, while solution aging or direct aging for a short duration improves mechanical properties. Further, the majority of Cr elements were precipitated within the grain boundaries providing more grain boundary reinforcement. Therefore, an increase in the strength of this part is expected.<sup>[49]</sup> The interface had also gone through morphological changes. It is observed that the interface in Figure 6b gained more uniformity after the heat treatment and the dendrites dissolved into smaller morphologies. IN718 also showed partial dissolution of interdendritic regions into the Ni matrix and formed islands containing MC carbides and Laves phase. Thus, the overgrown interdendrites during the production were eliminated, as seen in Figure 6c. It is worth noting that the direct aging at 480 °C for 2 h did not significantly change the size of the MC carbides and Laves in IN718.

The HT2 consists of a solution annealing and an aging stage resulted in severe grain coarsening for both of the materials. The solid-solution Cr-rich particles were dissolved into the copper matrix during the solution annealing stage and formed a supersaturated uniform microstructure. Afterwards, the Cr precipitated into the grain boundaries during the aging stage and formed a grain boundary reinforced microstructure. It is also obvious that the subsequent aging heat treatment did not cause dispersed Cr precipitation as observed in HT1 although the temperature and duration were similar. On the other hand, the Cr elements were precipitated within the grain boundaries, as shown in Figure 6d. Diaio et al.<sup>[50]</sup> also reported that 1 h solution

annealing followed by 2 h aging yields a similar supersaturated microstructure. The segregation of Cr elements within the grain boundaries affected by temperature and duration of the solution annealing post treatment, as discussed by Kuai et al.<sup>[51]</sup> The interface in Figure 6e shows changes in the morphology of the IN718 islands. As observed, there are two main types of islands namely, spherical and dendritic. It seems that the dendritic islands tended to grow toward the CuCrZr side and further decomposed into the spherical islands and coalescence to form larger parts. The IN718 side in Figure 6f also shows a dramatic change as the solution annealing stage was intense enough to completely dissolve the interdendritic region. Moreover, clusters of needle-like and bright particles were observed on the surface of the IN718 side. These particles are believed to be the  $\delta$  phase, which was also predictable from the time-temperature-transformation (TTT) diagram of this material.<sup>[52]</sup> The  $\delta$  phase contains a large amount of Nb and Mo, as previously highlighted in other studies.<sup>[44]</sup> The  $\pm 45^\circ$  orientation of the  $\delta$  phase brings high tensile strength due to its capability to hold dislocations from propagation.<sup>[52]</sup> The clusters of  $\delta$  were accompanied by 1–1.5  $\mu\text{m}$  MC carbides that also promote the mechanical properties of this alloy. Although it is known that the precipitation of  $\gamma' + \gamma''$  phase occurred during the aging at a minimum of 620 °C,<sup>[53]</sup> the partial precipitation of these phases is also observable after 480 °C aging in Figure 6f.

High-temperature solution annealing (i.e., HT3), led to the formation of large solid-solution particles within the Cu matrix



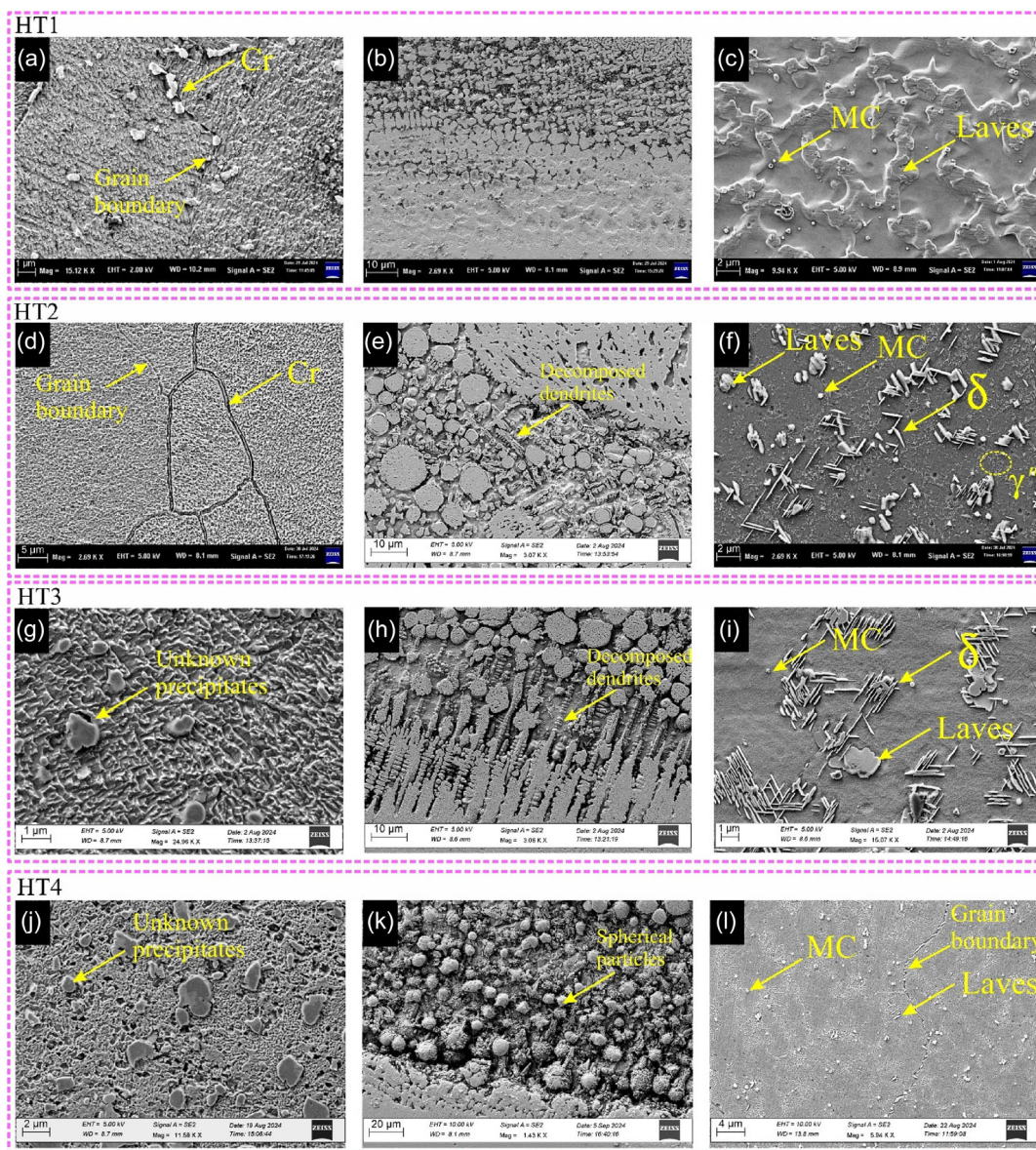


**Figure 6.** SEM micrographs from different locations of heat-treated samples: a–c) HT1, d–f) HT2, g–i) HT3, and j–l) HT4.

(see Figure 6g), which requires the EDS analysis for the composition determination. The interface in Figure 6h demonstrates a transition step from the decomposition of dendritic trees into amorphous IN718 islands. The high temperature put the copper alloy into a semi-melted condition, which provided IN718 more mobility and freedom to penetrate into the copper side. The base material penetrated into the interface region through elongated dendritic trees, which were further decomposed to independent fine particles. The IN718 material in Figure 6i revealed the dissolution of the interdendritic region at high temperatures, as also observed after HT2; however, the formation of dense  $\delta$  clusters was promoted. It can be seen in Figure 6i that the population of MC carbides decreased and no sign of the precipitation-hardening  $\gamma'/\gamma''$  phase exists within the Ni matrix, as previously demonstrated by Li et al.<sup>[54]</sup>

Upon performing triple aging post-treatment after a high-temperature annealing stage (i.e., HT4), major changes occurred on the CuCrZr side. Figure 6j shows the precipitation of large particles within the copper matrix; however, these particles are much larger than the previously observed Cr precipitates. Therefore, the EDS analysis is required to identify the composition of these precipitates. The interface in Figure 6k seems to experience full dendrite decomposition into fine island morphologies that are detached from the IN718 side. Afterward, high-temperature solution annealing almost melted the copper alloy, which gave freedom to the isolated IN718 islands to coalesce and form larger morphologies. This condition also provided favorable circumstances for the interface to extend further. On the other hand, IN718 microstructure showed considerable changes, as there was no sign of a coarse needle-like  $\delta$  phase. Instead, coarse



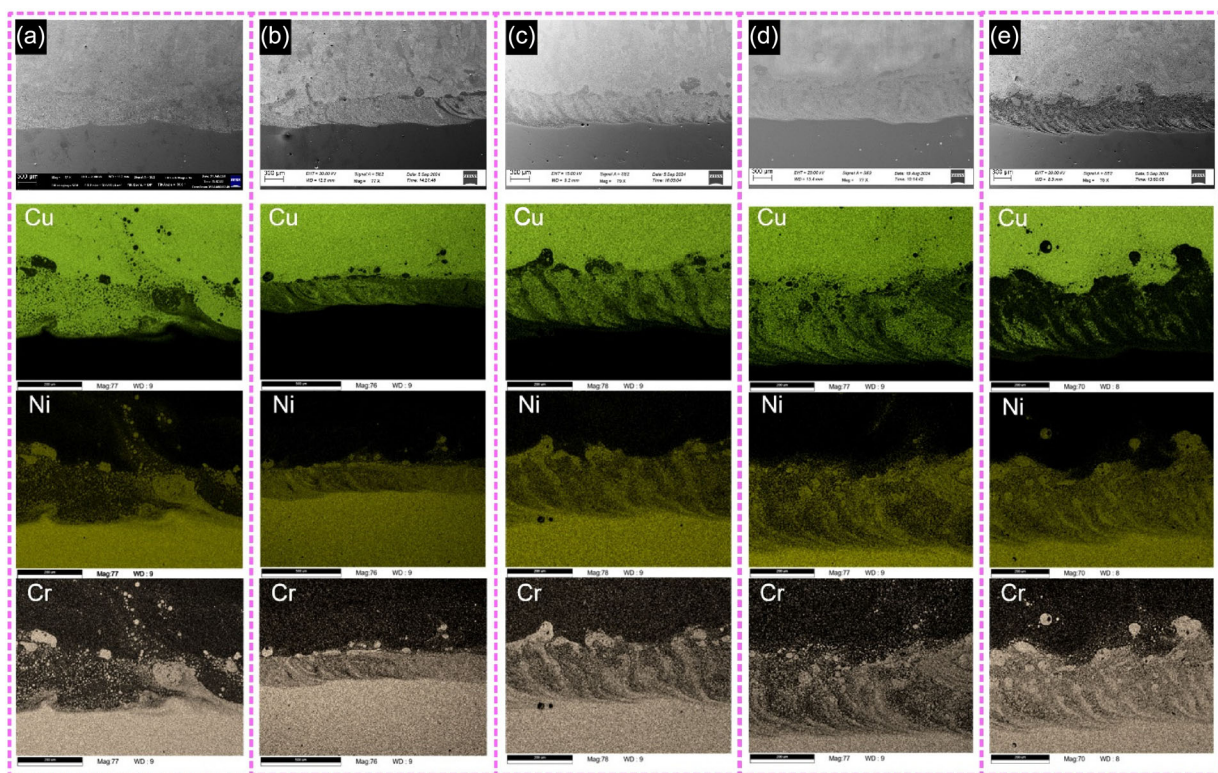
$\gamma'$ , and  $\gamma''$  phases with an average length of 250 nm can be observed, as shown in Figure 6l. Although the precipitation of MC carbides is expected, the formation of precipitates within the grain boundaries requires further investigation, as discussed in Section 3.4. The overall microstructure resembles  $\gamma$  and  $\gamma''$  with partial formation of the needle-like  $\delta$  phase. Therefore, it is expected to observe a considerable increase in the hardness of this sample. Nonetheless, the obtained phases in addition to  $\gamma$  were needle-like  $\delta$ , blocky Laves,  $\gamma'$ , and  $\gamma''$  as for the single-alloy heat treatment with similar steps.<sup>[54]</sup>

### 3.4. EDS and EBSD Analyses

Figure 7a–e show the EDS map from a random region in the vicinity of the interface area of the as-built and heat-treated conditions. As shown, the top region in all samples contains a large amount of Cu, which is an indication of CuCrZr, while the bottom region is abundant with Ni. The Cr content varied throughout the interface and is common in both alloys. It is obvious that the width and uniformity of the fusion zone increased after each stage of heat treatment. After the HT1, further diffusion of IN718 and CuCrZr occurred and formed a thicker and more uniform interfacial region. The same phenomenon was observed by Liu et al.<sup>[32]</sup> for the interface of steel and aluminum bronze alloy. The HT2 caused nucleation and progression of fish scales due to the applied high temperature. During the high-temperature heat treatment (i.e., HT3), the fish scales within the interface gained enough mobility to expand and decompose to spherical morphologies, which also gained density during prolonged exposure to

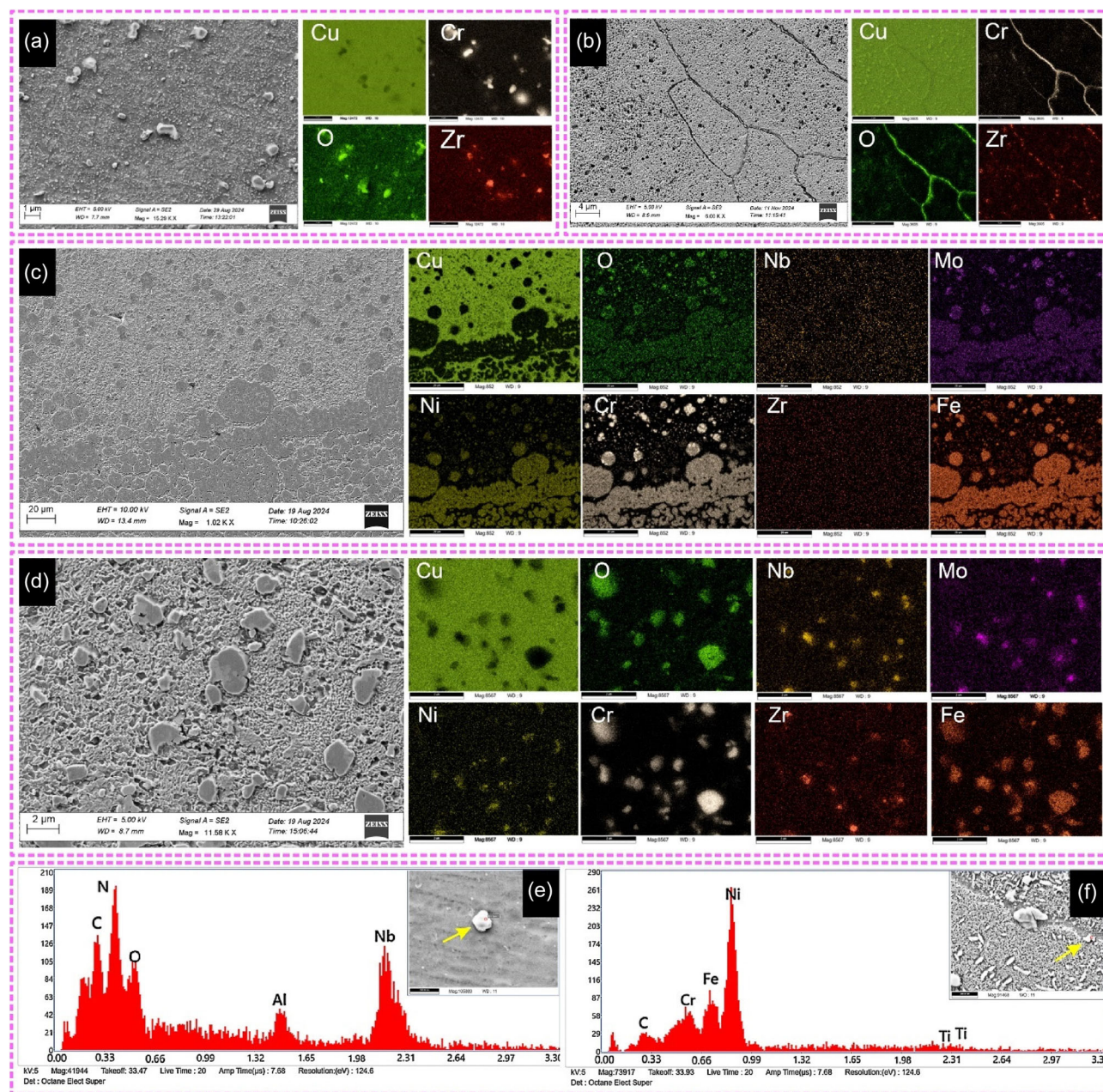
heat. During the aging stages in the HT4, the interface gained more density of IN718 as observed in the HT1. Therefore, the solution annealing led to the interface expansion while the aging post-process caused more uniformity.

Figure 8a was taken from the copper side of the bimetallic sample after the HT1. It can be seen that the Cr and Zr were concentrated in large solid-solution particles that also contain oxygen. Figure 8b shows the precipitation of Cr within the grain boundaries, which formed a uniform distribution after the HT2. Wang et al.<sup>[48]</sup> previously showed that the same temperature with half of the duration leads to discrete Cr precipitation. Therefore, longer exposure to heat provided more uniformity in Cr precipitation within the grain boundaries. The copper alloy showed enlarged precipitates after the HT3 and HT4 that were not likely to be just Cr; therefore, the EDS analysis was carried out to identify the composition of these precipitates. Figure 8c shows the obtained EDS map from the interface region of the HT3 sample. As found, the precipitates contained Cr, Fe, Mo, Zr, Nb, and a few Ni. The reason for this phenomenon is the convection of relatively low-density elements from IN718 toward the CuCrZr during the high-temperature solution annealing and the formation of concentrated precipitates within the copper matrix. This effect is due to the closeness of the annealing temperature to the melting point of copper, which provides enough mobility for the low-density elements to move freely within the matrix. The EDS data from the CuCrZr side of the HT4 sample in Figure 8d shows the same solid-solution elements far from the interface. The presence of oxygen in the precipitates is related to the production took place in an open environment, which resulted in an accelerated reaction of oxygen with chromium.



**Figure 7.** The EDS map from the CuCrZr/IN718 interface at different conditions: a) as-built, b) HT1, c) HT2, d) HT3, and e) HT4.





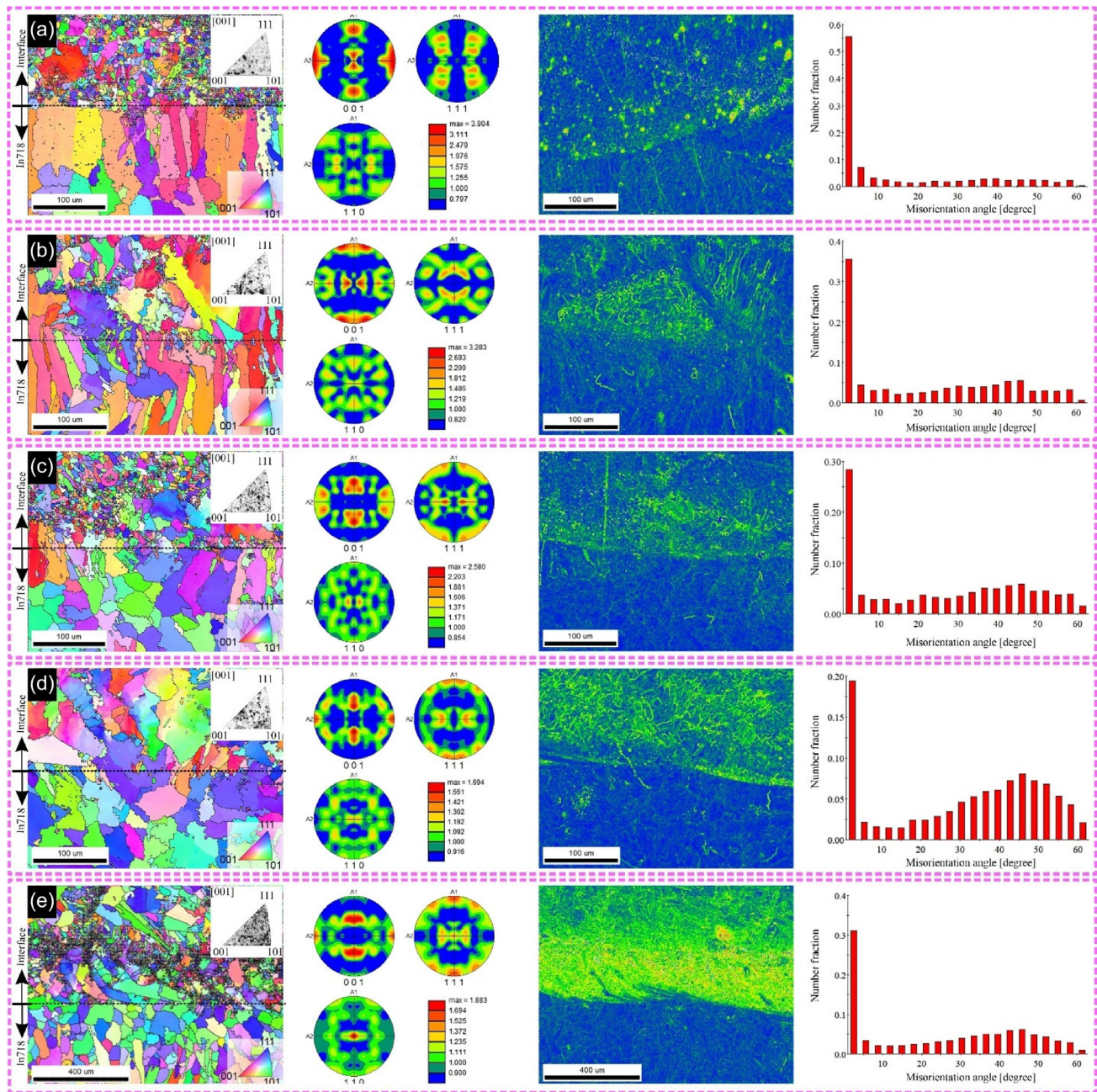
**Figure 8.** EDS map from the copper section: a) HT1, b) HT2, c) HT3, and d) HT4; spot EDS from IN718 side: e) as-built and f) HT4.

Figure 8e,f show the EDS point analysis of the precipitated carbides of IN718 in the as-built and HT4 conditions, respectively. It can be seen that the as-built carbide mainly contained Nb and Al, which are indications of the MC-type carbide.<sup>[55]</sup> The MC carbides are generally formed within the interdendritic region and remain consistent during annealing; therefore, it can be predicted that the majority of the carbides within the heat-treated samples are MC carbides. On the other hand, the  $M_{23}C_6$  carbide can be formed within the grain boundaries during prolonged heat treatment at moderate temperature (e.g., aging),<sup>[56]</sup> which was not the case in HT1 to HT3. The HT4 showed traces of Cr/Fe-rich precipitates within

the grain boundaries in Figure 8f, which revealed the presence of  $M_{23}C_6$  carbide as well.<sup>[55]</sup>

Figure 9a–e show the inverse pole figure (IPF) orientation, pole figure (PF), and kernel average misorientation (KAM) maps along with the grain boundary misorientation distribution taken from the interface of the as-built and heat-treated samples. In the as-built condition shown in Figure 10a, the majority of the grains tend to elongate in the Z direction, which is the preferred heat dissipation direction. The PF map also confirmed the domination of (001) direction with a maximum multiple of random distribution (MRD) of 3.904. However, signs of moderate grain orientation along the (111) and (101) directions suggest occasional randomness of the





**Figure 9.** The IPF, PF, KAM, and the grain misorientation angle distribution from the vertical cross-section of the interface at different conditions: a) as-built, b) HT1, c) HT2, d) HT3, and e) HT4.

grain growth due to the complex and rapid formation of the interface. Fine and small-angle grains with an average size of 5  $\mu\text{m}$  were found in the vicinity of the interface; however, larger grains up to 150  $\mu\text{m}$  were observed as getting far from the interface. Since the thermal conductivity of IN718 is far lower in comparison to the copper alloy, a lower cooling rate was observed during the deposition of CuCrZr on IN718. Therefore, coarser grains were formed as going further from the interface toward the top region. A distinguishable border can be observed between the CuCrZr and IN718, as previously observed by other

researchers.<sup>[42]</sup> The reason for grain refinement in the interface region is the formation of IN718 particles that act as the grain nucleation sites for CuCrZr alloy.<sup>[57]</sup>

Figure 9b shows the obtained map from the HT1 sample. It can be seen that grain coarsening and reorientation from (001) to (101) occurred in the interface region after direct aging at 480  $^{\circ}\text{C}$ . Since the major composition of the interface was copper, this effect was predictable. Wang et al.<sup>[58]</sup> showed that the grain coarsening occurred after direct aging of CuCrZr, and the crystal orientation shifted from (101) to (111). However, the IN718 side



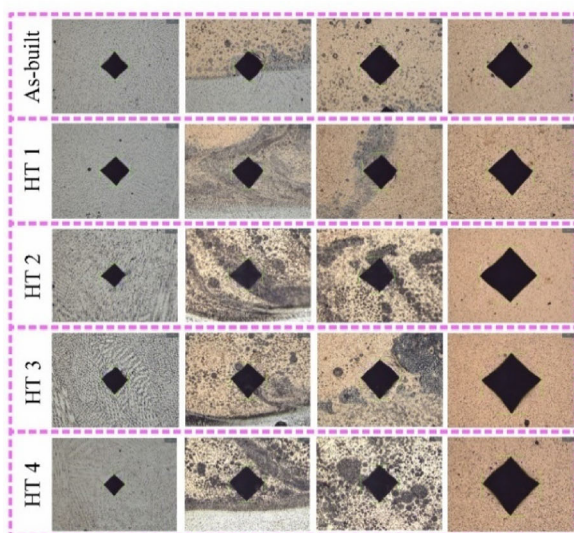
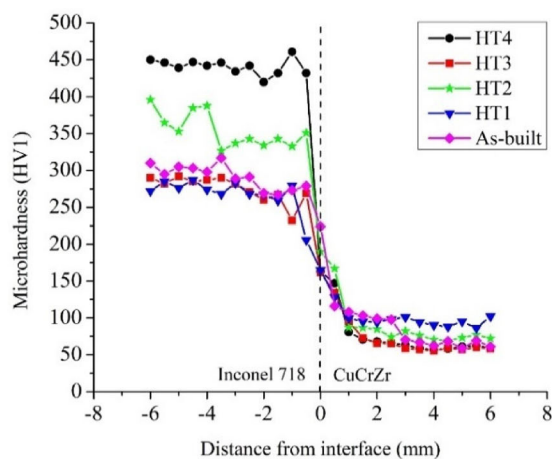


**Figure 10.** Microhardness test results with selected indentation micrographs from the as-built and heat-treated conditions.

showed no significant changes since the temperature was relatively lower than the recrystallization temperature for IN718. The PF data revealed that the reduction of the MRD to 3.282, which indicates an overall recrystallization after the HT1. The heat treatment seems to have partially annealed the structure, reducing the strong (001) orientation seen previously. Broader intensity distributions in all PFs and the weakened (001) orientation along with a more dispersed pattern in the (111) direction implied a slight increase in the randomness of the grains.

After the solution annealing at 980 °C and aging at 480 °C (i.e., HT2) in Figure 9c, the grains in the IN718 side went through major recrystallization and formed an equiaxed structure. It can be observed that the grain growth occurred throughout the interface and shaped a uniform microstructure. The overall IPF pattern suggested a balanced orientation of grains as expected from annealing heat treatment. After the high-temperature recrystallization of IN718 during the first stage, the grains were inactivated during the second stage (i.e., aging). On the other hand, the copper alloy continued to evolve even during the second stage, which caused grain refinement in the top region of the interface.

The regions with very fine grains formed due to the randomization of growth orientation and presence of a super-cooled and rigid IN718 contact, which promoted new grain formation at these regions. It is worth noting that the fish scales stood out with a very fine grain structure due to the mismatch in the cooling rate during the cooldown stage of the heat treatment. The PF data showed further reduction in the maximum MRD to 2.580 and a broader distribution in the (001) direction, which indicate more texture weakening in this direction. By considering the texture weakening in the other two direction and reduction in the intensity, a more isotropic structure was obtained.

Further, in Figure 9d, the HT3 with only a high-temperature annealing stage showed major grain growth throughout the interface and significant reorientation. The IPF plot indicates less textured grain structure and more dispersed growth direction. The PF maps reveal a lower maximum MRD of 1.694, which indicates less intensity for the specific planes and higher orientation randomness. The red region in the (001) direction became less concentrated and more diffuse compared to the previous cases. The observed very fine grains in the upper side of the interface after the HT2 had not been formed in this case due to the less time for individual recrystallization of the fish scales.

Lastly, the HT4 with a high-temperature annealing stage and triple aging sequence resulted in grain refinement in the IN718 side with a slight reorientation effect, as shown in Figure 9e. It can be concluded that the grains tended to reform along the (111) and (101) directions based on the FCC lattice structure. The annealing stage in HT4 caused major interface expansion while the subsequent aging decomposed the fish scales to separated islands. Very fine grains were formed within the thin fish scales, which acted as a grain nucleation point for the surrounding CuCrZr. By comparing the obtained results with the previously reported data after similar heat treatment temperatures with less duration,<sup>[48]</sup> it can be interpreted that the aging stage after solution annealing did not have a significant impact on the grain orientation of CuCrZr; however, the grain size was considerably coarser in the present study due to the prior annealing stage. Nevertheless, the grain refinement in the vicinity of IN718 fish scales was observed similar to the HT2 case but with higher severity due to the used triple aging heat treatment. In the PF maps the symmetric and diffused regions surrounding by the red regions reported a weak (001) alignment. The MRD was slightly increased to 1.883 resulted from the aging post-process, which still indicated a random grain growth.

The KAM map and misorientation angle histogram revealed high misorientation existed in the as-built interface due to the excessive residual stress generated during the deposition. Note that the difference in the thermal expansion behavior and high cooling rate were the main reasons for high residual stress in the vicinity of interface. It can be seen that the majority of grains possessed low angles of less than 15° caused by the formation of subgrains within the interface region. After heat treatment, the overall residual stress was relaxed and the misorientation density decreased on the IN718 side by increasing the heat treatment temperature or duration in HT1 and HT2. The HT2 revealed the least low-angle grains population since the annealing temperature was not too high to provide excessive mobility for IN718 to spread and also not too low to leave IN718 unaffected. However, the interface evolution during the heat



treatment caused local misorientation occurrence due to the growth of interdiffusion between IN718 and CuCrZr within the interface. This caused local stress induction during the solidification stage of heat treatment, as was also observed in the IPF maps. Unlike what was observed in heat-treated bronze-steel bimetallic structures,<sup>[32]</sup> the misorientation density increased by increasing the heat treatment stages. The reason for this finding is the thermal mismatch-induced stresses produced during various heat treatment stages and the inherent lattice mismatch, which causes subgrain formation. The difference between the thermal expansion coefficient caused significant thermal stress during the cooling stages. Therefore, the misorientation density increased in the interface by increasing the temperature and duration of heat treatment. Additionally, the phase transformation of IN718 in the vicinity of the interface along with the expansion of interface generated significant stress. Apart from the interface, the misorientation angle tends to move toward higher angles by increasing the annealing temperature, which acts similar to the pure materials.<sup>[59]</sup>

### 3.5. Microhardness Analysis

Figure 10 shows the Vicker's microhardness in the vicinity of the interface along the Z direction for the optimized interface in the as-built and heat-treated conditions. The maximum hardness value for the as-built sample was measured at 325 HV in the IN718 region, which was lower than the previously reported value for the same material.<sup>[60]</sup> Coarse grains and low dislocation density are the main reasons for this finding. For the bimetallic L-PBF IN718/CuCrZr, Zhang et al.<sup>[57]</sup> reported higher hardness for the IN718 due to the finer grain structure while the CuCrZr is almost at the same hardness range. As the indenter aimed toward the interface from the IN718, the hardness value first dropped to 260 HV and then increased just before entering the interfacial region. Grandhi et al.<sup>[61]</sup> observed an increase in the hardness of IN718 before the fusion zone with CuSn10. Since smaller grains were formed in the vicinity of the interface in the as-built condition, a higher hardness value was measured for the IN718 prior to the interface region. The as-built interface showed almost the average hardness value between the IN718 and CrCrZr, which was 220 HV. Above the fusion zone, there was a gradient grain size throughout the sample height, which was also revealed by the hardness variations. Depending on the size of the CuCrZr grains, the hardness varied from 105 to 80 HV. Since the grains were finer in the vicinity of the interface, higher hardness values were generally obtained.

After the HT1 heat treatment, a smoother hardness transition occurred due to the grain refinement within the interface. Grain growth led to a decrease in the hardness of IN718 while improving the hardness of CuCrZr to an average of 100 HV. Note that the aging strategy decreased the hardness of the interface to 165 resulting from the grain refinement. Despite the grain growth, the HT2 improved hardness to the average of 363 HV on the IN718 side due to the precipitation of solid-solution phases such as  $\gamma''$ ,  $\gamma'$ , and  $\delta$ . The sharp changes in the hardness values of HT2 IN718 resulted from the clash of the indenter with hard precipitates like the Laves and  $\delta$ . For CuCrZr, solution annealing at temperatures higher than 550 °C can significantly decrease hardness value.<sup>[62]</sup>

Although solution annealing can decrease the hardness down to 70 HV, direct aging or post-annealing aging can recover hardness up to 200 HV.<sup>[34,50,63]</sup> In the CuCrZr region, a more uniform hardness was observed (i.e.,  $\approx 85$  HV), which was generally higher than the as-built condition. Precipitation of the Cr element within the grain boundaries was the main reason behind the slight increase in the hardness of the CrCrZr alloy after the HT2. Homogenization heat treatment causes grain growth and dissolution of solid-solution phases; therefore, the hardness of IN718 is generally decreased.<sup>[64]</sup> Thus, the HT3 heat treatment showed a slight decrease in the hardness of the IN718 compared to the as-built condition. The excessive grain growth to an average of 60  $\mu\text{m}$  during the heat treatment caused a reduction in the hardness of CuCrZr to less than 70 HV, which is lower than the as-deposited condition. Through the HT4, a proper aging process leads to a uniform precipitation of the  $\gamma''$  and  $\gamma'$  phases, which significantly enhance the hardness of IN718.<sup>[16]</sup> Therefore, the IN718 side experienced superior hardness up to 461 HV after the HT4. However, this strategy did not affect the interface properties as expected and a similar hardness to the HT3 specimen was observed in the CuCrZr part.

## 4. Discussion

The interface between IN718 and CuCrZr showed a broad interdiffusion due to the high input heat. The key processing parameters, namely laser power and scan speed, have a significant impact on the formation of the interface. It was concluded that the increase of laser power increases the depth of melt pool penetration and adds more disturbance, which results in the formation of fish scales and spherical particles migrating from the base IN718 to the upper layers. At the same time, increasing the scan speed provides less time for the IN718 particles to adjust and join; therefore, smaller particles tend to form. In general, the formation of fish scales assists in stronger bonding between the two materials; however, it causes fluctuations in the mechanical properties of the interface. The dimensions of fish scales can also be engineered based on the application and materials by changing the laser power and scan speed.

Heat treatment is generally required for both IN718 and CuCrZr in order to improve their mechanical properties for specific applications. However, due to the misalignment between the standard heat treatment strategies for the two materials, a tradeoff point should be determined in order to achieve acceptable properties for both of the participants. It was shown that the HT2, which consists of a solution annealing and an aging stage can result in mechanical properties improvement for both of the materials. It was also observed that the mentioned heat treatment causes dendrite growth within the IN718 side of the fusion zone, which provides better bonding between the two materials. The EBSD analysis showed that the HT2 provided enough time and temperature for grain growth and interface uniformity. The optimum sample after the HT2 revealed an average microhardness of 363 and 85 HV in the IN718 and CuCrZr sides, respectively.

A closer look at the interface after the over-etching of the copper alloy provides a deeper understanding of the formation and evolution of the interface. **Figure 11** shows the evolution of the interface from the IN718 perspective in the as-built and

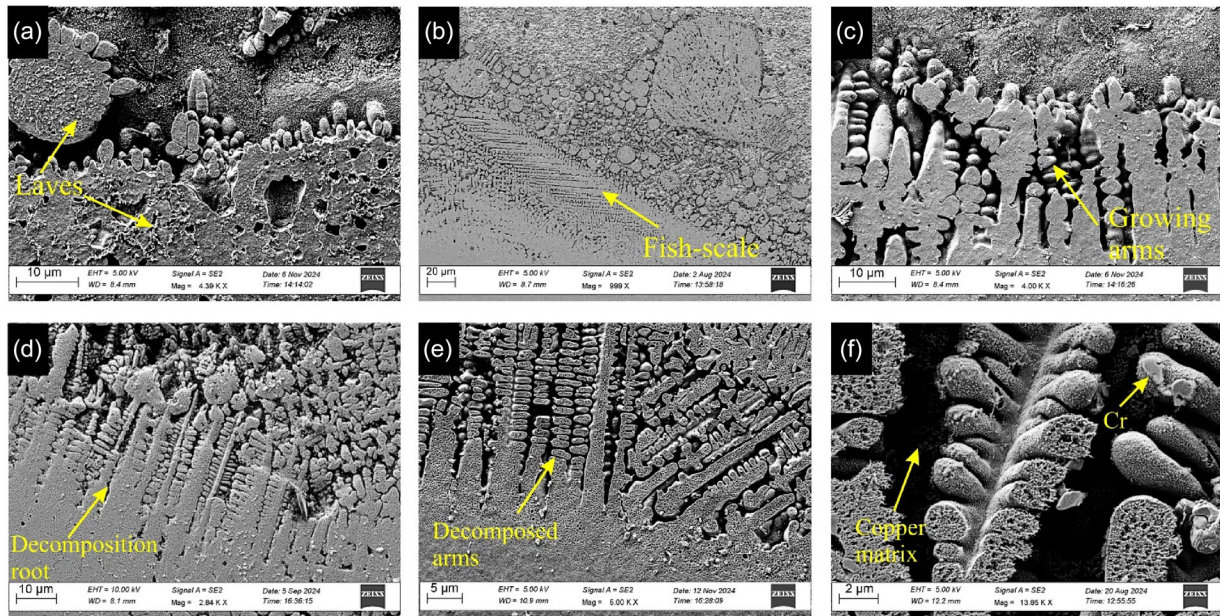


**Figure 11.** Closer look at the IN718/CuCrZr interface: a) as-built, b,c) HT2, d) HT3, and e,f) HT4.

heat-treated conditions. It can be seen in Figure 11a that the population of the Laves phase is higher in the vicinity of the interface, which also justifies the sudden jump in the hardness value prior to the interface region. Furthermore, the dendrite sprouts can be observed within the interface boundary, which results from the relatively high local cooling rate. After the heat treatment, the interface started to evolve and the dendrites grew toward the copper part. Upon applying HT2 in Figure 11b,c, which provided higher mobility dendrites growth was accelerated and released fine spherical particles through decomposition. It was observed that the fish scale structures broke down into dendritic trees and later departed as islands at higher temperatures during the HT3, as shown in Figure 11d. The higher temperatures close to the melting point of copper showed near-complete decomposition of fish scales and the formation of elongated dendritic trees, as well as a high density of islands. This phenomenon continued by increasing the duration of heat treatment via triple aging in the HT4 (Figure 11e,f). This heat treatment strategy also caused the progressive decomposition of fish scales toward the root inside the IN718 base. This means that the base IN718 decomposed into dendrites and formed fine arms, which were surrounded by liquid copper during the high-temperature exposure.

## 5. Conclusions

This work delivered a comprehensive investigation of the production of IN718/CuCrZr bimetallic structures via the LP-DED method. The effect of process parameters and post-processing treatments on the formation and evolution of the interface was demonstrated. Microstructural and mechanical characterization indicated the sensitivity of the interface to the manufacturing parameters and the applied heat treatment. It was shown that the optimum process parameters lead to mixed spherical and fish

scale morphologies within the interface while applying heat treatment expands the interface through mass transport. The mechanical properties of the interface decreased after the heat treatments due to the grain coarsening and reorientation effect. The hardness of IN718 can be significantly improved by solution annealing and aging; however, the hardness of CuCrZr cannot be extensively improved. Overall, the HT2 led to an improved microstructure and hardness for both materials; thus, it is recommended prior to the implementation of such coating or bimetallic components.

## Acknowledgements

The authors would like to thank SENTES BIR for providing the CuCrZr powder used in this study. This research received an external funding from the Scientific and Technological Research Council of Turkey (TUBITAK) [grant number: 121D021 – 3219504/35].

## Conflict of Interest

The authors declare no conflict of interest.

## Author Contributions

**Hamidreza Javidrad:** conceptualization (equal); data curation (lead); formal analysis (lead); investigation (lead); methodology (lead); validation (lead); visualization (lead); writing—original draft (lead); writing—review and editing (equal). **Bahattin Koc:** conceptualization (equal); funding acquisition (lead); project administration (lead); resources (lead); software (equal); supervision (lead); writing—review and editing (equal).

## Data Availability Statement

The data that support the findings of this study are available from the corresponding author upon reasonable request.



## Keywords

additive manufacturing, bimetallic fabrication, heat treatment, interface, material characterization

Received: March 28, 2025  
Revised: June 13, 2025  
Published online: July 15, 2025

- [1] H. Javidrad, H. Aydin, B. Karakaş, S. Alptekin, A. S. Kahraman, B. Koc, *Opt. Laser Technol.* **2024**, 176, 110940.
- [2] S. Salemi, H. Javidrad, *J. Mater. Eng. Perform.* **2021**, 30, 3761.
- [3] M. Riahi, H. Javidrad, *Russ. J. Nondestr. Test.* **2020**, 56, 843.
- [4] Y. Hu, W. Cong, *Ceram. Int.* **2018**, 44, 20599.
- [5] B. Ringel, M. Zaepfel, F. Herlan, M. Horn, M. Schmitt, C. Seidel, *Mater. Today. Proc.* **2022**, 70, 296.
- [6] X. Zhang, L. Li, F. Liou, *J. Mater. Res. Technol.* **2021**, 15, 2045.
- [7] J. Kar, S. K. Roy, G. G. Roy, *J. Mater. Process. Technol.* **2016**, 233, 174.
- [8] D. Feenstra, R. Banerjee, H. Fraser, A. Huang, A. Molotnikov, N. Biribilis, *Curr. Opin. Solid State Mater. Sci.* **2021**, 25, 100924.
- [9] K. Makarenko, I. Shishkovsky, *IOP Conf. Seri.: Mater. Sci. Eng.* **2020**, 969, 012104.
- [10] P. Yang, D. He, S. Lu, S. Chen, D. Oleksandr, X. Guo, *J. Mater. Res. Technol.* **2024**, 28, 4350.
- [11] U. Articek, M. Milfelner, I. Anzel, *Adv. Prod. Eng. Manage.* **2013**, 8, 169.
- [12] P. R. Gradl, S. Greene, T. Wammen, in *AIAA Propulsion and Energy 2019 Forum*, Indianapolis IN **2019**, pp. 4361.
- [13] B. Onuiki, B. Heer, A. Bandyopadhyay, *Addit. Manuf.* **2018**, 21, 133.
- [14] S. Karnati, Y. Zhang, F. F. Liou, J. W. Newkirk, *Metals* **2019**, 9, 287.
- [15] E. L. Stevens, J. Toman, A. C. To, M. Chmielus, *Mater. Des.* **2017**, 119, 188.
- [16] L. Alqawasmi, S. T. Bijjala, T. Khraishi, P. Kumar, *J. Mater. Sci.* **2024**, 59, 5047.
- [17] Z. Kuai, Z. Li, B. Liu, Y. Chen, S. Lu, X. Tang, T. Liu, *J. Mater. Res. Technol.* **2022**, 19, 4915.
- [18] J. Chen, J. Wang, X. Xiao, H. Wang, H. Chen, B. Yang, *Mater. Sci. Eng., A* **2019**, 756, 464.
- [19] Z. Li, M. Zhou, K. Jing, Y. Liu, G. Xin, H. Hu, J. Zou, B. Tian, Y. Zhang, X. Li, *Mater. Today Commun.* **2024**, 38, 108408.
- [20] R. Anderson, J. Terrell, J. Schneider, S. Thompson, P. Gradl, *Metall. Mater. Trans. B* **2019**, 50, 1921.
- [21] W. Zhang, B. Zhang, H. Xiao, H. Yang, Y. Wang, H. Zhu, *Micromachines* **2021**, 12, 1394.
- [22] Z. Liu, D. Zhang, S. Sing, C. Chua, L. Loh, *Mater. Charact.* **2014**, 94, 116.
- [23] S. Mao, D. Z. Zhang, Z. Ren, G. Fu, X. Ma, *J. Alloys Compd.* **2022**, 899, 163256.
- [24] J. Chen, Y. Yang, C. Song, M. Zhang, S. Wu, D. Wang, *Mater. Sci. Eng., A* **2019**, 752, 75.
- [25] J. Chen, Y. Yang, C. Song, D. Wang, S. Wu, M. Zhang, *Mater. Sci. Eng., A* **2020**, 792, 139316.
- [26] J. Chen, M. Zhang, D. Zhao, G. Bi, Y. Bai, Y. Xiao, D. Wang, *Mater. Charact.* **2024**, 211, 113862.
- [27] H. Yang, Z. Tang, L. Wan, Q. Wei, J. Wu, A. Wang, X. Jin, X. Li, Y. Wu, G. Lu, *J. Alloys Compd.* **2023**, 931, 167572.
- [28] A. Mishra, A. R. Paul, M. Mukherjee, R. K. Singh, *Met. Mater. Int.* **2023**, 29, 2331.
- [29] T. Pan, X. Zhang, T. Yamazaki, A. Sutton, W. Cui, L. Li, F. Liou, *Int. J. Adv. Manuf. Technol.* **2020**, 109, 1261.
- [30] M. Cabibbo, A. Fava, R. Montanari, E. Pakhomova, C. Paoletti, M. Richetta, A. Varone, *J. Mater. Sci.* **2022**, 57, 1.
- [31] H. Javidrad, S. Salemi, *Metall. Mater. Trans. A* **2020**, 51, 5880.
- [32] J. Liu, Y. Miao, Z. Wang, Y. Zhao, Y. Wu, C. Li, *Mater. Charact.* **2024**, 207, 113462.
- [33] Y. Li, M. Koukolíková, J. Džugan, M. Brázda, *Mater. Sci. Eng., A* **2024**, 898, 146389.
- [34] X. Zhang, Q. Lei, M. T. Andani, X. Liu, H. Zhang, W. Wang, Y. Li, Y. Yang, *Mater. Chem. Phys.* **2023**, 298, 127477.
- [35] J. Schneider, B. Lund, M. Fullen, *Addit. Manuf.* **2018**, 21, 248.
- [36] N. Jeyaprakash, I. A. Alnaser, Y. Cheng, S. S. Karuppasamy, *Tribol. Int.* **2024**, 197, 109826.
- [37] Z. Hu, Z. Ma, L. Yu, Y. Liu, *Scr. Mater.* **2023**, 226, 115197.
- [38] X. Dang, Y. Li, K. Chen, S. Luo, X. Liang, W. He, *Mater. Des.* **2022**, 216, 110595.
- [39] W. Q. Zhang, B. P. Zhang, H. F. Xiao, H. H. Zhu, *Mater. Sci. Forum* **2022**, 1054, 31.
- [40] M. Koukolíková, T. Simson, S. Rzepa, M. Brázda, J. Džugan, *J. Mater. Sci.* **2022**, 57, 13695.
- [41] L. Li, Q. Wang, K. Wang, W. Wang, Y. Zhang, X. Zhang, *Mater. Sci. Eng., A* **2024**, 907, 146557.
- [42] K. Liu, Z. Yan, R. Pan, X. Wang, F. Wang, S. Chen, *Mater. Sci. Eng., A* **2024**, 898, 146381.
- [43] A. Munitz, *Metall. Trans. B* **1987**, 18, 565.
- [44] H. Javidrad, M. Isik, B. Koc, *J. Alloys Compd.* **2024**, 1004, 175805.
- [45] S. Zhang, L. Wang, X. Lin, H. Yang, W. Huang, *Composites, Part B* **2022**, 239, 109994.
- [46] S. Sreekanth, K. Hurtig, S. Joshi, J. Andersson, *J. Laser Appl.* **2021**, 33, 022024.
- [47] A. Devaux, L. Nazé, R. Molins, A. Pineau, A. Organista, J. Guédou, J. Uginet, P. Héritier, *Mater. Sci. Eng., A* **2008**, 486, 117.
- [48] Q. Wang, J. Song, W. Wang, Y. Zhang, K. Wang, Z. Du, *Adv. Eng. Mater.* **2024**, 26, 2301680.
- [49] C. Wallis, B. Buchmayr, *Mater. Sci. Eng., A* **2019**, 744, 215.
- [50] Z. Diao, F. Yang, Y. Zhang, L. Chen, T. Xiong, W. Yang, M. Rong, *J. Alloys Compd.* **2023**, 967, 171786.
- [51] Z. Kuai, Z. Li, B. Liu, Y. Chen, S. Lu, P. Bai, *J. Mater. Res. Technol.* **2023**, 23, 2658.
- [52] A. A. Alafaghani, M. A. Ablat, H. Abedi, A. Al Gamal, A. Qattawi, *JOM* **2022**, 74, 4772.
- [53] Y. Zhou, X. Fang, N. Xi, X. Jin, K. Tang, Z. Zhang, Q. Zhang, Y. Yang, K. Huang, *J. Mater. Sci. Technol.* **2024**, 199, 86.
- [54] P. Li, J. Zhou, Y. Gong, X. Meng, J. Lu, *J. Mech. Sci. Technol.* **2021**, 35, 2871.
- [55] N. C. Ferreri, S. C. Vogel, M. Knezevic, *Mater. Sci. Eng., A* **2020**, 781, 139228.
- [56] L. Emanuelli, F. Deirmina, M. Pellizzari, *Mater. Charact.* **2023**, 199, 112788.
- [57] L. Zhang, P. Dong, Y. Zeng, H. Yao, J. Chen, *Addit. Manuf.* **2024**, 92, 104377.
- [58] Q. Wang, Y. Zhang, K. Wang, S. Liu, X. Zhang, H. Shao, *Mater. Sci. Eng., A* **2022**, 857, 144054.
- [59] E. M. Fayed, M. Saadati, D. Shahriari, V. Brailovski, M. Jahazi, M. Medraj, *Sci. Rep.* **2021**, 11, 2020.
- [60] L. Chechik, K. A. Christofidou, J. F. Markanday, A. D. Goodall, J. R. Miller, G. West, H. Stone, I. Todd, *Materialia* **2022**, 26, 101643.
- [61] M. Grandhi, V. Nguyen, Z. Liu, C.-O. Romo-De-La-cruz, X. Song, *J. Manuf. Process.* **2023**, 100, 47.
- [62] H. Feng, H. Jiang, D. Yan, L. Rong, *Trends J. Sci. Res.* **2019**, 4, 1.
- [63] X. Tang, X. Chen, F. Sun, L. Li, P. Liu, H. Zhou, S. Fu, A. Li, *J. Alloys Compd.* **2022**, 924, 166627.
- [64] P. Ramiro, H. Galarraga, A. Pérez-Checa, M. Ortiz, A. Alberdi, T. Bhujangrao, E. Morales, E. Ukar, *Metals* **2022**, 12, 952.